Portland State University

PDXScholar

Spring 6-2024

PT-Symmetry and Eigenmodes

Tamara Gratcheva
Portland State University

Follow this and additional works at: https://pdxscholar.library.pdx.edu/honorstheses

Part of the Analysis Commons, Atomic, Molecular and Optical Physics Commons, Numerical Analysis and Computation Commons, Optics Commons, and the Other Mathematics Commons

Let us know how access to this document benefits you.

Recommended Citation

PT-symmetry and eigenmodes

by

Tamara Gratcheva

An undergraduate honors project submitted
in partial fulfillment of the requirements for the

Fariborz Maseeh Department of Mathematics and Statistics
Honors Track

Under the supervision of
Prof. Jay Gopalakrishnan

Portland State University

July 16, 2024

PT-symmetry and eigenmodes

Abstract

Spectra of systems with balanced gain and loss, described by Hamiltonians with parity and time-reversal (PT) symmetry is a rich area of research. This work studies by means of numerical techniques, how eigenvalues and eigenfunctions of a Schrödinger operator change as a gain-loss parameter changes. Two cases on a disk with zero boundary conditions are considered. In the first case, within the enclosing disk, we place a parity (P) symmetric configuration of three smaller disks containing gain and loss media, which does not have PT-symmetry. In the second case, we study a PT-symmetric configuration of two smaller disks with gain and loss media. We find a rich variety of exceptional points, re-entrant PT-symmetric phases, and a non-monotonic dependence of the PT-symmetry breaking threshold on the system parameters. Previous explorations of spectra of PT-symmetric systems have mainly been limited to finite discrete models or problems in one dimension. By leveraging systems on a two-dimensional continuum, we show how the complexity and variability of the spectral behavior increases. Finally, by considering small analytically computable examples, we study the concept of exceptional points and their relation to the PT-symmetry breaking threshold.

1 Introduction

In this thesis, we study the behavior of eigenvalues and eigenfunctions of partial differential operators arising from models with two types of symmetry. The first symmetry is reflection symmetry about an axis, or parity ($\mathcal{P}$) symmetry. The second is symmetry under the composition of parity and time-reversal operations, known as PT-symmetry. The latter case has received considerable attention in the literature on "non-Hermitian physics" due to its striking applications.

Over the past 25 years research on non-Hermitian Hamiltonians with real spectra has become an area of focus across disparate topics in physics, spanning mathematical physics [1]–[4], optics and photonics [5], [6], acoustics [7], electrical circuits [8], [9], condensed matter physics [10], [11], and open quantum systems [12]–[16]. Beginning with Bender and Boettcher's discovery [17] that the Schrödinger eigenvalue problem for a non-relativistic particle on an infinite line with complex potentials $V(x) = V_R(x) + iV_I(x)$ has purely real spectrum, and is bounded below. Similar results are obtained for non-relativistic particle on a line with compact support [18], [19], discrete tight-binding models on finite or infinite lattices [20]–[22], and even minimal models with 2×2 Hamiltonians. In each case, the non-Hermitian Hamiltonian H, which is typically an unbounded operator or a matrix, commutes under the combined operations of parity P and time-reversal $\mathcal{T}$. This antilinear PT-symmetry guarantees purely real or complex conjugate eigenvalues [23], as we shall see in detail later.

After their experimental realizations in numerous platforms, it has become clear that PT-symmetric Hamiltonians accurately model open systems with balanced, spatially separated gain ($V_I > 0$) and loss ($V_I < 0$) [24]. If we begin from the Hermitian Hamiltonian H_0

with real spectrum and orthogonal eigenfunctions, as the imaginary part of the potential $V_I(x)$ is increased, two or more purely real eigenvalues will develop into complex-conjugate pairs. This eigenvalue degeneracy, called exceptional point (EP) degeneracy [25]–[27], is characterized by the coalescence of corresponding eigenfunctions and lowering of the rank of the Hamiltonian operator. The transition across the EP from a real spectrum to one with complex-conjugate eigenvalues is called the PT-symmetry breaking transition, since the corresponding eigenfunctions lose that symmetry, i.e., $PTu(x) \neq u(x)$.

We will investigate a two-dimensional continuum model on a compact domain subject to hard-wall (vanishing eigenfunctions) boundary condition in the presence of constant PT-symmetric complex-valued potentials. In one dimension, such potential leads to a single PT-symmetry breaking transition when the strength of the imaginary part of the potential, γ, exceeds a threshold $\gamma_P T$ set by the Hermitian Hamiltonian H_0. We will show that the two-dimensional case differs dramatically. It leads to multiple transitions where pairs of stable eigenmodes change into amplifying and leaky eigenmodes (complex conjugate eigenvalues) as γ is increased. Moreover, we find PT-reentrant behavior where, as the pure gain-loss potential V_I is increased, amplifying and leaky modes become stable again (purely real eigenvalues). This complex behavior can be further explained by varying the sizes and distances of the subdomains.

This thesis is structured as follows. In Section 2, through elementary mathematical arguments, we understand that commuting operators preserve each other's eigenspaces. We then use this fact to study the parity and PT symmetric configurations in Sections 3 and 4. In Section 5, we outline of the numerical procedure we use for discretization. Results on the spectra, including eigenfunctions, for both our P-symmetric model of Section 6, as well as our PT-model of Section 4, across multiple PT-breaking and restoring transitions are collected in Section 7. Finally, Section 8 concludes the paper with a discussion on exceptional points and their relation to our results. Note that the original numerical findings obtained during this work, described in Section 7, are also being published in a journal paper [28]. The materials in the remaining sections do not substantial overlap with this publication.

2 Commuting operators

Let X be a vector space over $\mathbb{C}$, and consider the following linear operator, $A : X \to X$. A nonzero $u \in X$, satisfying $Au = \lambda u$ for some $\lambda \in \mathbb{C}$ is called an *eigenvector,* and λ is called the corresponding *eigenvalue.* We define the corresponding *eigenspace* E_λ^A by $E_\lambda^A = \{u \in X : Au = \lambda u\}$.

A subspace $U \subseteq X$ is called an *invariant subspace* of A if

$$AU \subseteq U,$$

where $AU = \{Au : u \in U\}$. The eigenspace E_λ^A is an invariant subspace of A, i.e,

$$AE_\lambda^A \subseteq E_\lambda^A. \tag{1}$$

Indeed, (1) is immediately seen; let $x \in E_\lambda^A$, and $y = Ax$. Then, $Ay = A(Ax) = A(\lambda u) = \lambda y$. In other words, $y \in E_\lambda^A$, thus showing that $AE_\lambda^A \subseteq E_\lambda^A$.

Next, consider an additional linear operator, $B : X \to X$, with the added property that *A and B commute,* which we write as

$$AB = BA. \tag{2}$$

For linear operators on a finite dimensional space (those given by matrices) or for *bounded* linear operators A, B on an infinite dimensional space X, this means that

$$ABu = BAu, \qquad \text{for all } u \in X. \tag{3}$$

We also allow linear operators A on X which are defined only on a subspace $\mathrm{dom}(A) \subset X$ called the domain of A. A subspace $U \subset X$ is invariant under an unbounded A if $A(U \cap \mathrm{dom}\, A) \subset U$. Eigenvector and eigenspaces of unbounded operators are, by definition, contained in their domain. An unbounded linear operator A is said to commute with a bounded linear operator B [25, p. 171] if whenever u is in $\mathrm{dom}(A)$, the vector Bu is also in $\mathrm{dom}(A)$ and

$$ABu = BAu, \qquad \text{for all } u \in \mathrm{dom}(A). \tag{4}$$

Thus, to summarize, *when we write* (2), *we mean that either* (3) *holds or* (4) *holds* depending on whether A is bounded or unbounded, respectively.

Next, let us discuss the often-made statement that "commuting operators preserve each other's eigenspaces." More precisely, we prove the following result.

Proposition 2.1. *If* (2) *holds, then every eigenspace of A is an invariant subspace of B.*

Proof. We need to prove that when A and B commute,

$$BE_\lambda^A \subseteq E_\lambda^A. \tag{5}$$

Consider an eigenvector $x \in E_\lambda^A$. Then, since $Ax = \lambda x$, applying B to both sides, $BAx = B\lambda x$. By commutativity, $ABx = \lambda Bx$. This shows that $Bx \in E_\lambda^A$. Hence (5) holds. $\square$

Corollary 2.2. *Suppose* (2) *holds and* $\dim E_\lambda^A = 1$. *Then, given any eigenvector $x \in E_\lambda^A$, the vector Bx is a scalar multiple of x.*

Proof. For any $x \in E_\lambda^A$, applying B to $Ax = \lambda x$, we get $BAx = B\lambda x$, or $ABx = \lambda Bx$, by commutativity. Thus both x and Bx are in the eigenspace E_λ^A, which is given to be of dimension one. Hence, they must be collinear. $\square$

The final result needed is for the case when B is an *antilinear* bounded operator instead of a linear operator as assumed above, i.e., for $\alpha \in \mathbb{C}$ and $x, y \in X$, the operator has the property that

$$B(\alpha x + y) = \bar{\alpha} Bx + By.$$

The definition of commutativity of an antilinear B with a (bounded or unbounded) linear operator A is exactly the same as what we have described above.

Proposition 2.3. *If an antilinear bounded operator B and a linear operator A satisfy the commutativity property* (2), *then the following statements hold:*

1. If λ is a real eigenvalue of A and x is a corresponding eigenvector, then both x and Bx are in E_λ^A. In particular if $\dim E_\lambda^A = 1$, then both x and Bx are collinear.

2. If λ is a complex eigenvalue of A and x is a corresponding eigenvector, then $\bar{\lambda}$ must be an eigenvalue of A and Bx must be a corresponding eigenvector.

Proof. Given that $Ax = \lambda x$ for some $x \in X$, applying B to both sides,

$$BAx = B\lambda x = \bar{\lambda} Bx$$

by the antilinearity of B. Hence, by commutativity,

$$ABx = \bar{\lambda} Bx.$$

Both statements of the proposition follow as a result. $\square$

3   Parity Symmetry

In this section, we describe a commonly occurring symmetry operator that commutes with a differential operator. Let $\Omega \subset \mathbb{R}^2$ be a bounded domain with Lipschitz boundary with *reflection symmetry* about the second axis, i.e., any point in Ω when reflected about the second axis also lies in Ω, and

$$\{(-x_1, x_2) :\ (x_1, x_2) \in \Omega\} = \Omega.$$

Let $L^2(\Omega)$ denote the set of complex-valued functions f on Ω whose absolute value $|f|$ is square integrable on Ω. Define the *parity operator* $P : L^2(\Omega) \to L^2(\Omega)$ by

$$(Pf)(x_1, x_2) = f(-x_1, x_2),$$

i.e., P mirrors functions on Ω about the second axis. Let $(\cdot, \cdot)$ denote the (complex) $L^2(\Omega)$-inner product, that is, given $u, v \in L^2(\Omega)$, their inner product is given by the integral

$$(u, v) = \int_\Omega u(x_1, x_2)\, \bar{v}(x_1, x_2)\, dx_1 dx_2. \tag{6}$$

The accompanying norm is $\|u\| = (u, u)^{1/2}$. By a change of variable in the integrals, using the reflection symmetry of Ω, one can prove that for all $u, v \in L^2(\Omega)$,

$$\begin{aligned} (Pu, v) &= (u, Pv), \\ \|Pu\| &= \|u\|, \end{aligned} \tag{7}$$

i.e., P is a linear, self-adjoint, and unitary operator in $L^2(\Omega)$.

Next, consider the Laplacian operator, denoted by Δ, on this domain, supplemented with zero boundary conditions. It is an unbounded linear operator on $L^2(\Omega)$ with

$$\mathrm{dom}(\Delta) = H^2(\Omega) \cap \mathring{H}^1(\Omega) \subset L^2(\Omega). \tag{8}$$

Here, we use standard notation (see [29]–[31]) for Sobolev spaces $H^k(\Omega)$ of complex-valued functions and the subspace $\mathring{H}^1(\Omega)$ of $H^1(\Omega)$-functions with zero boundary values in the appropriate sense.
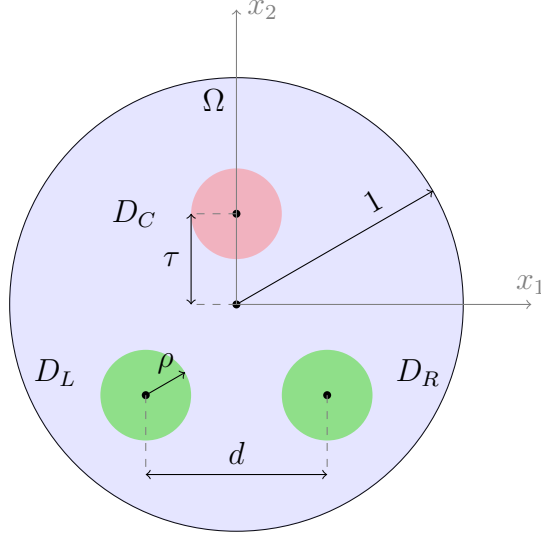
Figure 1: An example with reflection symmetry (P-symmetry). Geometrical parameters of this P-symmetric model are the domain Ω of radius 1, gain medium (green) subdomains D_L and D_R of radii ρ, placed d units apart, and a balanced lossy (red) medium subdomain D_C.

Lemma 3.1. *The parity operator P and the Laplacian Δ commute, i.e, $\Delta P = P\Delta$.*

Proof. Per (4), we must prove that whenever $u \in \mathrm{dom}(\Delta)$, the function Pu is also in $\mathrm{dom}(\Delta)$ and that $\Delta Pu = P\Delta u$ holds.

Let $u \in \mathrm{dom}(\Delta)$. By the chain rule,

$$\frac{\partial}{\partial x_1} u(-x_1, x_2) = -\frac{\partial u}{\partial x_1}(-x_1, x_2).$$

i.e., $\partial_{x_1} Pu = -P\partial_{x_1} u$. Additionally, $\partial_{x_2} Pu = P\partial_{x_2} u$. Thus, Pu is in $H^1(\Omega)$ if and only if u is in $H^1(\Omega)$. Higher order derivatives can be similarly treated. Hence, $Pu \in \mathrm{dom}(\Delta)$.

By repeated application of chain rule,

$$
\begin{aligned}
(\Delta Pu)(x_1, x_2) &= \left(\frac{\partial^2}{\partial x_1^2} + \frac{\partial^2}{\partial x_2^2} \right) u(-x_1, x_2) \\
&= \left(\frac{\partial^2 u}{\partial x_1^2} + \frac{\partial^2 u}{\partial x_2^2} \right)(-x_1, x_2) = (P\Delta u)(x_1, x_2),
\end{aligned}
$$

thus proving the result. $\qquad\square$

Consider the problem of finding a nontrivial complex-valued eigenfunction u on Ω and a complex number λ such that

$$\mathcal{H}u = \lambda u, \qquad\qquad \text{in } \Omega, \tag{9a}$$

$$u = 0, \qquad\qquad \text{on the boundary } \partial\Omega, \tag{9b}$$

where

$$\mathcal{H} = -\Delta u + Vu. \tag{10}$$

We say $\mathcal{H}$ is *P-symmetric* if

$$P\mathcal{H} = \mathcal{H}P. \tag{11}$$

Note that $\mathcal{H} = -\Delta u + Vu$ is an unbounded operator on $L^2(\Omega)$ with $\text{dom}(\mathcal{H}) = \text{dom}(\Delta)$ as specified in (8). Suppose

$$V(-x_1, x_2) = V(x_1, x_2), \qquad (x_1, x_2) \in \Omega, \tag{12}$$

i.e., the potential V is reflection-symmetric. If we also denote the operator $u \mapsto Vu$ by simply V, we make the following elementary observation.

Lemma 3.2. *Suppose* (12) *holds. Then the parity operator P commutes with the V operator.*

Proof. Similar to the proof of Lemma 3.1, we begin by applying P to Vu, to see $P(Vu) = V(-x_1, x_2)u(-x_1, x_2)$. By (12), since $V(-x_1, x_2) = V(x_1, x_2)$, we immediately have

$$P(Vu)(x_1, x_2) = V(x_1, x_2)\,(Pu)(x_1, x_2).$$

Thus, V and P commute. $\qquad\square$

Proposition 3.3. *If P is the parity operator, $\mathcal{H}$ is as defined in* (10) *on a reflection-symmetric Ω, and V satisfies* (12), *then $\mathcal{H}P = P\mathcal{H}$.*

Proof. Let $u \in \text{dom}(\mathcal{H})$. It is easy to verify that $Pu \in \text{dom}(\mathcal{H})$. By applying P to the definition $\mathcal{H}u = -\Delta + Vu$,

$$P\mathcal{H}u = P(-\Delta u + Vu)$$
$$= -\Delta Pu + P(Vu) = \mathcal{H}Pu,$$

by Lemma 3.1 and Lemma 3.2. $\qquad\square$

Corollary 3.4. *Under the assumptions of Proposition 3.3, if $x \in E_\lambda^{\mathcal{H}}$, then $Px \in E_\lambda^{\mathcal{H}}$.*

Proof. This follows immediately from Proposition 2.1 since $\mathcal{H}$ and P commute by Proposition 3.3. $\qquad\square$

The significance of Corollary 3.4 is that *any eigenfunction of $\mathcal{H}$ after reflection continues to be an eigenfunction of $\mathcal{H}$ with the same eigenvalue λ.* In particular, if the eigenspace of λ is one-dimensional, as in Corollary 2.2, then eigenfunctions of the eigenvalue λ must be reflection-symmetric.

We conclude this section with a particular example of $\mathcal{H}$, a Schrödinger operator that we will focus on later for further study. Let $\mathcal{B}_r(p_1, p_2) = \{(x_1, x_2) \in \mathbb{R}^2 : (x_1 - p_1)^2 + (x_2 - p_2)^2 < r^2\}$ denote the disk of radius r centered at p, where $p = (p_1, p_2) \in \mathbb{R}^2$ and put

$$\Omega = \mathcal{B}_1(0, 0).$$

We see this Ω is reflection-symmetric. The potential V is illustrated by the configuration in Figure 1, and is defined using a real parameter γ by

$$V(x_1, x_2) = \begin{cases} 1 + \gamma i, & \text{if } (x_1, x_2) \in D_L, D_R \\ 1 - 2\gamma i, & \text{if } (x_1, x_2) \in D_C, \\ 1, & \text{otherwise,} \end{cases} \tag{13}$$

7

where D_L, D_R, and D_C are the subdomains indicated in Figure 1, and i is the imaginary unit. Clearly, the property (12) holds for this V. Hence, Proposition 3.3 and Corollary 3.4 holds for this example. If we model optical fibers with three cores, two of which balance out the third, the configuration of Figure 1 can arise. This Schrödinger operator $\mathcal{H}$ then arises when simplifying the time-harmonic Maxwell system using the translational symmetry of the fiber to compute the so-called TM modes: see e.g., the derivation in [29, Lecture Notebook G].

4 PT-Symmetry

In this section, we consider the problem of finding a nontrivial complex-valued function u on Ω and a complex number λ such that

$$\mathcal{A}u = \lambda u, \qquad \text{in } \Omega, \tag{14a}$$
$$u = 0, \qquad \text{on the boundary } \partial\Omega, \tag{14b}$$

where $\mathcal{A} = -\Delta u + Vu$. This is a similar type of Schrödinger operator as in the previous section, differing only in that V is no longer reflection symmetric. Instead, the operator $u \mapsto Vu$ (which we continue to denote by V) commutes with an antilinear operator. We will describe this through the following example, which we will study in further detail.
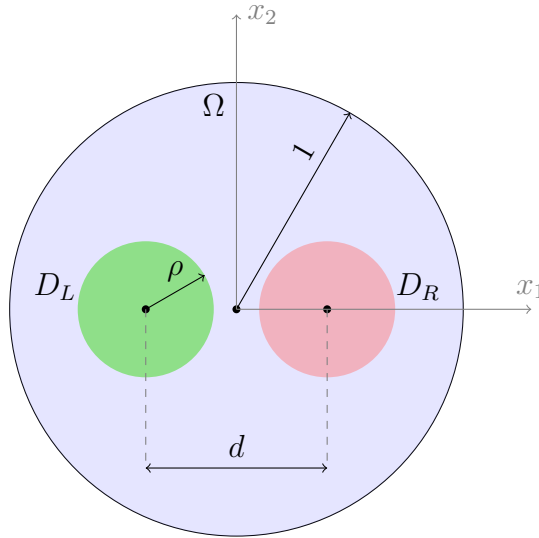

Figure 2: An example of PT symmetry. Geometrical parameters of this P symmetric model are the domain Ω of radius 1, gain medium (green) subdomain D_L and a lossy medium (red) subdomain D_R of radii ρ, placed d units apart.

Given a configuration like Figure 2, we set V using a given real parameter γ by

$$V(x_1, x_2) = \begin{cases} 1 - \gamma i, & \text{if } (x_1, x_2) \in D_R \\ 1 + \gamma i, & \text{if } (x_1, x_2) \in D_L \\ 1, & \text{otherwise,} \end{cases} \tag{15}$$

8

where D_L, D_R are as indicated in Figure 2, and i is the imaginary unit.

Let $T : L^2(\Omega) \to L^2(\Omega)$ be the antilinear operator given by

$$(Tf)(x_1, x_2) = \overline{f(x_1, x_2)}.$$

Here, the overline indicates complex conjugation. This T is often called the *time-reversal operator*. This terminology can be understood from the time-harmonic ansatz. Namely, given a real-valued function $\hat{f}(x, t)$ of space x and time t, suppose its time variation is harmonic. Meaning, there is a complex-valued $f(x)$ satisfying

$$\hat{f}(x, t) = \mathrm{Re}(f(x)e^{i\omega t})$$
$$= \frac{1}{2}(f(x)e^{i\omega t} + \overline{f(x)}e^{-i\omega t}).$$

Now, if we change the sign of t, then

$$\hat{f}(x, -t) = \frac{1}{2}(f(x)e^{-i\omega t} + \overline{f(x)}e^{i\omega t})$$
$$= \mathrm{Re}(\overline{f(x)}e^{i\omega t}).$$

Therefore, time-reversal of $\hat{f}$ in the time-harmonic regime is expressed simply by the complex conjugation of f.

The composition $P \circ T$, simply written as PT, is antiunitary. An operator H is said to be *PT-symmetric* if (2) holds with $A = H$ and $B = PT$, i.e.,

$$PTH = HPT. \tag{16}$$

Of interest to us is the (unbounded) operator $\mathcal{A}$ defined by

$$\mathcal{A}u = -\Delta u + Vu$$

for all $u \in \mathrm{dom}(\mathcal{A}) := H^2(\Omega) \cap \mathring{H}^1(\Omega)$. Here, $H^k(\Omega)$ denotes the Sobolev space of square-integrable functions, all of whose derivatives of order at most $k \geq 1$ are also square integrable, and $\mathring{H}^1(\Omega)$ denotes the subspace of $H^1(\Omega)$-functions that vanish on the boundary $\partial\Omega$.

Lemma 4.1. *The Laplacian Δ commutes with PT, i.e, $\Delta\,(PT) = (PT)\,\Delta$.*

Proof. By the results of Lemma 3.1, we already see that P commutes with Δ. Therefore, let us just show that T commutes with Δ. Let u be a complex-valued function on Ω. We see that

$$\Delta(PT)\,u(x_1, x_2) = \left(\frac{\partial^2}{\partial x_1^2} + \frac{\partial^2}{\partial x_2^2}\right)(PT)\,u(x_1, x_2).$$

Again, by repeated application of the chain rule, and recalling that Δ and P commute, we get

$$\Delta(PT)\,u(x_1, x_2) = \frac{\partial^2}{\partial x_1^2}(-x_1, x_2) + \frac{\partial^2}{\partial x_2^2}(Tu)(-x_1, x_2),$$
$$= \frac{\partial^2\overline{u}}{\partial x_1^2}(-x_1, x_2) + \frac{\partial^2\overline{u}}{\partial x_2^2}(-x_1, x_2),$$
$$= PT(\Delta u)(x_1, x_2).$$

In conclusion, $\Delta(PT) = (PT)\Delta$. $\qquad\qquad\square$

9

Lemma 4.2. *The potential V, as defined in (15), commutes with PT.*

Proof. We prove this similarly to Lemma 4.1, and use the results of Lemma 3.2. We compute

$$
\begin{aligned}
V(PTu)(x_1, x_2) &= V(x_1, x_2)\,\overline{u}(-x_1, x_2) \\
&= \overline{V}(-x_1, x_2)\,\overline{u}(-x_1, x_2) \\
&= PT(Vu)(x_1, x_2),
\end{aligned}
$$

where we used that $\overline{V}(-x_1, x_2) = V(x_1, x_2)$. Therefore, we have that $V(PT) = (PT)V$. $\quad\square$

Proposition 4.3. *Let V be as defined in (15) and $\mathcal{A} = -\Delta + V$. Then*

$$
PT\mathcal{A} = \mathcal{A}PT. \tag{17}
$$

Consequently, for every eigenvalue λ of $\mathcal{A}$ with corresponding eigenfunction $u \in \mathrm{dom}(\mathcal{A})$, the following statements hold:

1. *If λ is a real eigenvalue, then both u and PTu are in $E_\lambda^{\mathcal{A}}$. In particular if $\dim E_\lambda^{\mathcal{A}} = 1$, then both u and PTu are collinear.*

2. *If λ is a complex eigenvalue, then $\bar{\lambda}$ must be an eigenvalue of A having PTu as its eigenfunction.*

Proof. The commutativity (17) is an immediate consequence of Lemmas 4.1 and 4.2. The remaining statements then follow from Proposition 2.3 setting the antilinear operator B to PT. $\quad\square$

5 Numerical discretization by finite element method

The starting point [29], [31] for a Galerkin discretization of a partial differential operator is a weak formulation. We can develop the weak form using integration by parts. Given smooth complex-valued functions u, v defined on Ω, by the integration by parts formula, we have

$$
\int_\Omega \nabla u\,\overline{\nabla v}\,dx_1 dx_2 + \int_\Omega \Delta u\,\overline{v}\,\,dx_1 dx_2 = \int_{\partial\Omega} \nu \cdot \nabla u\,\overline{v}\,ds,
$$

where ν is the unit outward normal vector to $\partial\Omega$. Using the notation for L^2 inner product defined in (6), for any smooth test function v vanishing on the boundary $\partial\Omega$, this gives $(\Delta u, v) + (\nabla u, \nabla v) = 0$. Thus,

$$
\begin{aligned}
(\mathcal{A}u, v) &= (-\Delta u + Vu, v) \\
&= (-\Delta u, v) + (Vu, v) \\
&= (\nabla u, \nabla v) + (Vu, v).
\end{aligned}
$$

Therefore, the equation $\mathcal{A}u = \lambda u$ (see (14)) implies that for all such v,

$$
(\nabla u, \nabla v) + (Vu, v) = \lambda(u, v). \tag{18}
$$

10

This is the *weak formulation* of the eigenvalue equation $\mathcal{A}u = \lambda u$.

The finite element method imposes the same equation on the *Lagrange finite element* space X_h consisting of continuous functions, vanishing on $\partial\Omega$, which are polynomials of degree at most p in each mesh element. Here, the mesh is a geometrically conforming mesh of triangles subdividing the domain, respecting the material interfaces, with curved elements near the circular boundaries and interfaces. The subscript h indicates the maximal diameter of all elements in the mesh. Consequently, as h becomes smaller, or as p becomes larger, the discretization becomes finer and $\dim X_h$ becomes larger.

Our numerical method computes the eigenvalues of a discretization $\mathcal{A}_h : X_h \to X_h$ of the infinite-dimensional operator $\mathcal{A}$, defined by

$$(\mathcal{A}_h u_h, v_h) = (\nabla u_h, \nabla v_h) + (V u_h, v_h)$$

for all $u_h, v_h \in X_h$. Namely, we compute an eigenvalue approximation λ_h and eigenfunction u_h satisfying

$$\mathcal{A}_h u_h = \lambda_h u_h. \tag{19}$$

The (right) eigenfunction $u_h \in X_h$ in (19) is equivalently given by

$$(\mathcal{A}_h u_h, v_h) = \lambda_h (u_h, v_h),$$

for all $v_h \in X_h$.

To distinguish between the two main examples of potentials we focus on, let us denote by $\mathcal{H}_h : X_h \to X_h$ as the operator arising from the reflection-symmetric potential, namely

$$(\mathcal{H}_h w_h, v_h) = (\nabla w_h, \nabla v_h) + (V w_h, v_h) \qquad \text{with } V \text{ as in (13)}, \tag{20}$$

and $\mathcal{A}_h$ as the operator on X_h defined using the potential which is not reflection symmetric, namely,

$$(\mathcal{A}_h w_h, v_h) = (\nabla w_h, \nabla v_h) + (V w_h, v_h) \qquad \text{with } V \text{ as in (15)}, \tag{21}$$

for all $w_h, v_h \in X_h$.

Both of these discretized operators are defined on general finite element meshes without any symmetry constraints. As the maximal diameter of mesh elements denoted by h goes to 0, we expect discrete eigenvalues and eigenfunctions converge to their exact counterparts under further conditions. This can be seen in our numerical experiments. Proving this using finite element theory appears to be possible, but is beyond the scope of this thesis.

The case of reflection symmetric meshes offer further interesting applications of our prior discussions. Examples of such meshes are shown in Figure 3. We created such meshes using the Netgen mesh generator [32]. Since it does not have a built-in option to create symmetric meshes, we wrote a script which uses Netgen to mesh the right half of the domain, then reflect each mesh entity (elements, edges, points, labels, etc) about the vertical axis, and merge the halves into a consistent Netgen mesh structure. As we shall see now, on such reflection-symmetric meshes, the resulting discrete operators preserve commutativity and accompanying spectral structures that we saw previously for the exact (undiscretized) operators.

Lemma 5.1. *Suppose the mesh is reflection symmetric and let u_h and v_h be in the Lagrange space X_h with respect to such a mesh. Then the following holds:*
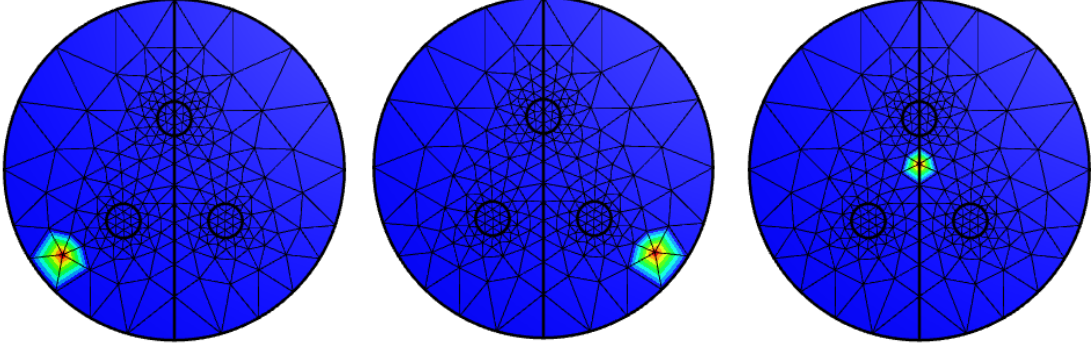
Figure 3: An example of a reflection-symmetric mesh and illustration of basis functions (finite element shape functions) of the Lagrange space on such a mesh. The last plot shows a reflection-symmetric shape function, where the reflection of the shape function in the first plot is the shape function in the second plot.

1. $Pu_h \in X_h$ and $Tu_h \in X_h$.

2. $(Pu_h, v_h) = (u_h, Pv_h)$.

3. $(\nabla Pu_h, \nabla v_h) = (\nabla u_h, \nabla Pv_h)$.

4. $(Tu_h, v_h) = \overline{(u_h, Tv_h)}$.

5. $(\nabla Tu_h, \nabla v_h) = \overline{(\nabla u_h, \nabla Tv_h)}$.

Proof.

(1). We can see that each basis function of the Lagrange space, upon an application of P, is either unchanged or results in another basis function of X_h, due to the symmetry of the mesh (the former case is illustrated in the last plot of Figure 3).

(2). The second statement follows from the first and by noting that

$$\int_\Omega (Pu_h)(x_1, x_2)v_h(x_1, x_2) \ dx_1 dx_2 = \int_\Omega u_h(-x_1, x_2)v_h(x_1, x_2) \ dx_1 dx_2,$$

and by changing the variable x_1 to $-x_1$,

$$\int_\Omega (Pu_h)(x_1, x_2)v_h(x_1, x_2) \ dx_1 dx_2 = \int_\Omega u_h(x_1, x_2)v_h(-x_1, x_2) \ dx_1 dx_2,$$

$$= \int_\Omega u_h(x_1, x_2) \ (Pv_h)(x_1, x_2) \ dx_1 dx_2,$$

so $(Pu_h, v_h) = (u_h, Pv_h)$.

(3). The proof of the third statement follows in a similar manner, with an additional application of the chain rule:

$$\int_\Omega (\nabla Pu_h)(x_1, x_2)\overline{\nabla v_h}(x_1, x_2) \ dx_1 dx_2 = \int_\Omega \begin{pmatrix} -\partial_{x_1} u_h(-x_1, x_2) \\ \partial_{x_2} u_h(-x_1, x_2) \end{pmatrix} \cdot \overline{\nabla v_h(x_1, x_2)},$$

$$= \int_\Omega \left(\frac{-\partial u_h}{\partial x_1}\right)(-x_1, x_2)\left(\frac{\partial \bar{v}_h}{\partial x_1}\right)(x_1, x_2) + \left(\frac{\partial u_h}{\partial x_2}\right)(-x_1, x_2)\left(\frac{\partial \bar{v}_h}{\partial x_2}\right)(x_1, x_2) \ dx_1 dx_2,$$

12

which after performing the change of variable $(x_1 \to -x_1)$, simplifies to

$$\int_\Omega \nabla u_h(x_1, x_2)(\overline{\nabla Pv_h}) \ dx_1 dx_2.$$

Thus we see that $(\nabla Pu_h, \nabla v_h) = (\nabla u_h, \nabla Pv_h)$.

(4). We see that

$$\int_\Omega (Tu_h)(x_1, x_2) \ v_h(x_1, x_2) \ dx_1 dx_2 = \int_\Omega \overline{u_h(x_1, x_2)\overline{v_h(x_1, x_2)}} \ dx_1 dx_2,$$

which becomes

$$(Tv_h, u_h) = \overline{(u_h, Tv_h)},$$

as desired.

(5). The proof of this item follows after using the fact that differentiation and conjugation commute. $\qquad\square$

Using the lemma, we now proceed to prove two results concerning the commutativity of the bounded operators $\mathcal{A}$ and $\mathcal{H}$ with the appropriate symmetry operators on the finite-dimensional space X_h.

Proposition 5.2. *Assume that the mesh is reflection symmetric. Then $P\mathcal{H}_h = \mathcal{H}_h P$ on X_h.*

Proof. To prove this, we use the earlier results as follows. For any $u_h, v_h \in X_h$,

$$
\begin{aligned}
(P\mathcal{H}_h u_h, v_h) &= (\mathcal{H}_h u_h, Pv_h) & \text{by Lemma 5.1(2),} \\
&= (\nabla u_h, \nabla Pv_h) + (Vu_h, Pv_h) & \\
&= (\nabla Pu_h, \nabla v_h) + (PVu_h, v_h), & \text{by (7) and Lemma 5.1(3),} \\
&= (\nabla Pu_h, \nabla v_h) + (VPu_h, v_h), & \text{by Lemma 3.2.}
\end{aligned}
$$

This proves that

$$(P\mathcal{H}_h u_h, v_h) = (\mathcal{H}_h Pu_h, v_h)$$

for all $u_h, v_h \in X_h$, as desired. $\qquad\square$

Proposition 5.3. *Assume that the mesh is reflection symmetric. Then $PT\mathcal{A}_h = \mathcal{A}_h PT$ on X_h.*

Proof. We prove this similarly to Proposition 5.2. For any $u_h, v_h \in X_h$,

$$
\begin{aligned}
(PT\mathcal{A}_h u_h, v_h) &= (T\mathcal{A}_h u_h, Pv_h), & \text{by Lemma 5.1(2),}\\
&= \overline{(\mathcal{A}_h u_h, TPv_h)}, & \text{by Lemma 5.1(4),}\\
&= \overline{(\mathcal{A}_h u_h, PTv_h)}, & \text{since } P \text{ and } T \text{ commute,}\\
&= \overline{(\nabla u_h, \nabla PTv_h) + (Vu_h, PTv_h)}\\
&= \overline{(\nabla Pu_h, \nabla Tv_h) + (PVu_h, Tv_h)} & \text{by Lemma 5.1(3),}\\
&= (\nabla PTu_h, \nabla v_h) + (PTVu_h, v_h) & \text{by Lemma 5.1(4),}\\
&= (\nabla PTu_h, \nabla v_h) + (VPTu_h, v_h) & \text{by Lemma 4.2,}\\
&= (\mathcal{A}_h PTu_h, v_h),
\end{aligned}
$$

which proves the stated commutativity on the space X_h. $\qquad\square$

The previous results show the following structure-preservation properties for symmetric meshes. The commutativity property $\mathcal{H}P = P\mathcal{H}$ (from the undiscretized case Proposition 3.3) is inherited by the discrete case, $\mathcal{H}_h P = P\mathcal{H}_h$ (seen in Proposition 5.2). The commutativity property $\mathcal{A}PT = PT\mathcal{A}$ (from the undiscretized case Proposition 4.3) is inherited by the discrete case as $\mathcal{A}_h PT = PT\mathcal{A}_h$ (seen in Proposition 5.3). Therefore we are able to apply the general results from Section 2 to the discretization for these cases.

We conclude this section with a final word on the numerical methodology we used for solving the discrete eigenproblems. All eigenproblems in this paper are being numerically solved using a contour integral eigensolver, known as FEAST [33], [34]. This iterative eigensolver solves the eigenproblem for a selected cluster of eigenvalues, within a contour. FEAST is also capable of computing its corresponding eigenmodes. This algorithm is suitable for not only Hermitian, but also non-Hermitian structures such as the ones considered in this paper. The numerical results presented in the following sections have been computed using an open-source implementation of FEAST in Python [35], built atop the open-source finite element library NGSolve [36]. We use NGSolve's mesh and solution visualization capabilities to report plots of finite element functions that represent eigenmodes of the P and PT symmetric models. We use standard Python visualization tools such as matplotlib for plots like band diagrams and eigenflows.

6 Results from the P-symmetric model

In this section, we report on our computations of the spectrum of the discretized operator $\mathcal{H}$ in (20).

Let us begin with the base case of $\gamma = 0$, or $V = 1$, from (13). In this case, solutions can be computed semi-analytically without any numerical computation. Eigenfunctions admit the separable form $u(r, \theta) = R(r)\Theta(\theta)$ in polar coordinates r, θ, where

$$
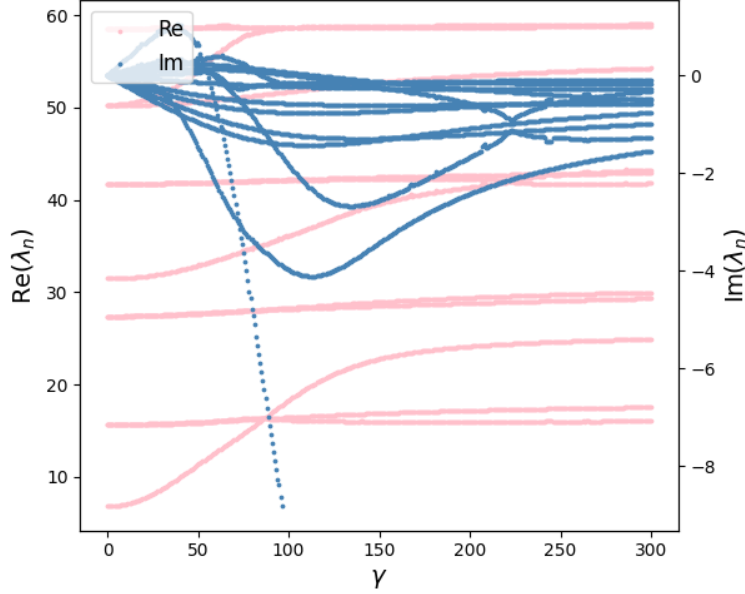R(r) = J_n(r\sqrt{\lambda - 1}), \qquad \Theta(\theta) = e^{in\theta},
$$

Figure 4: Bands showing the variations in the first seven eigenvalues as the parameter γ increases. Here, $d, \tau = 0.3$, and $\rho = 0.1$.

for some integer n. The boundary condition $u|_{\partial\Omega} = 0$ implies $J_n(\sqrt{\lambda - 1}) = 0$, which yields expressions for eigenvalues λ in terms of the ℓth zero $\mu_{n,\ell}$ of J_n. Namely, λ is one of

$$\lambda_{n,\ell} = 1 + \mu_{n,\ell}^2, \qquad n = 0, 1, 2, \ldots, \ \ell = 1, 2, \ldots. \tag{22}$$

In particular, the lowest seven eigenvalues in ascending order are

$$\begin{aligned}
\lambda_{0,1} &\approx 6.783, \\
\lambda_{1,1} &\approx 15.682 \text{ (multiplicity 2)}, \\
\lambda_{2,1} &\approx 27.375 \text{ (multiplicity 2)}, \\
\lambda_{0,2} &\approx 31.471, \\
\lambda_{3,1} &\approx 41.707 \text{ (multiplicity 2)}, \\
\lambda_{1,2} &\approx 50.219 \text{ (multiplicity 2)}, \\
\lambda_{4,1} &\approx 58.523 \text{ (multiplicity 2)},
\end{aligned} \tag{23}$$

and further eigenvalues can be easily generated from the Bessel zeros by the formula (22).

The semi-analytically-found eigenvalues at $\gamma = 0$ provide input initial locations for computing eigenvalue trajectories as γ increases. They also serve to verify our numerical methodology—our numerically computed eigenvalues were observed to be very close to the exact semi-analytically found values in the $\gamma = 0$ case. How each eigenvalue changes as γ increases from zero is shown in Figure 4. Where the eigenvalue bands in Figure 4 intersect the $\gamma = 0$ axis, the computed values are very close to the above listed semi-analytically found values. Afterward, as γ increases, we no longer have an analytical representation of the eigenvalues. The initially real eigenvalues become complex as γ increases. From the plots of the imaginary parts in Figure 4, the complex eigenvalues clearly do *not* appear to
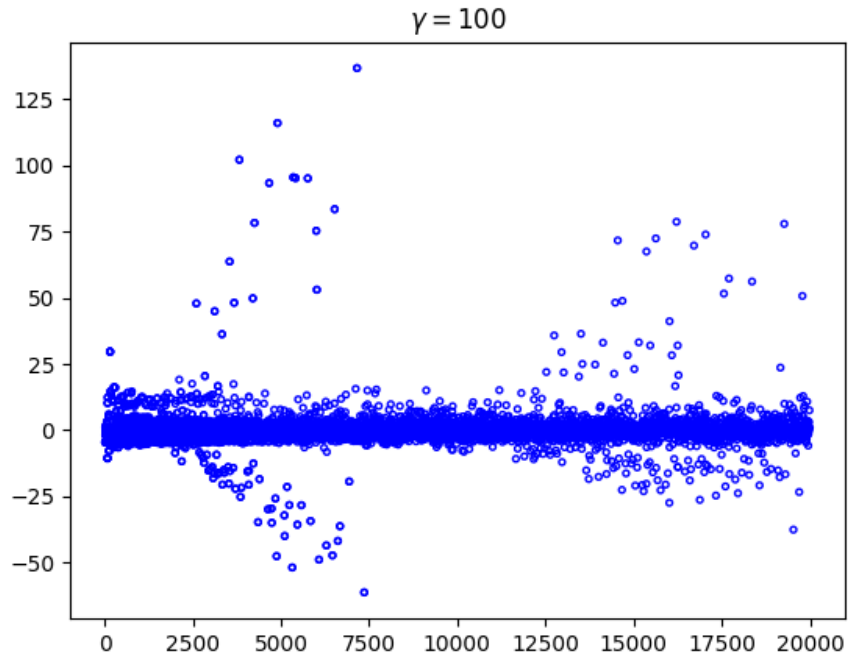
15

Figure 5: All solutions for a P symmetric model at $\gamma = 100$, of order 4. Here, $d, \tau = 0.3$, and $\rho = 0.1$. Not all complex eigenvalues appear as complex conjugate pairs.
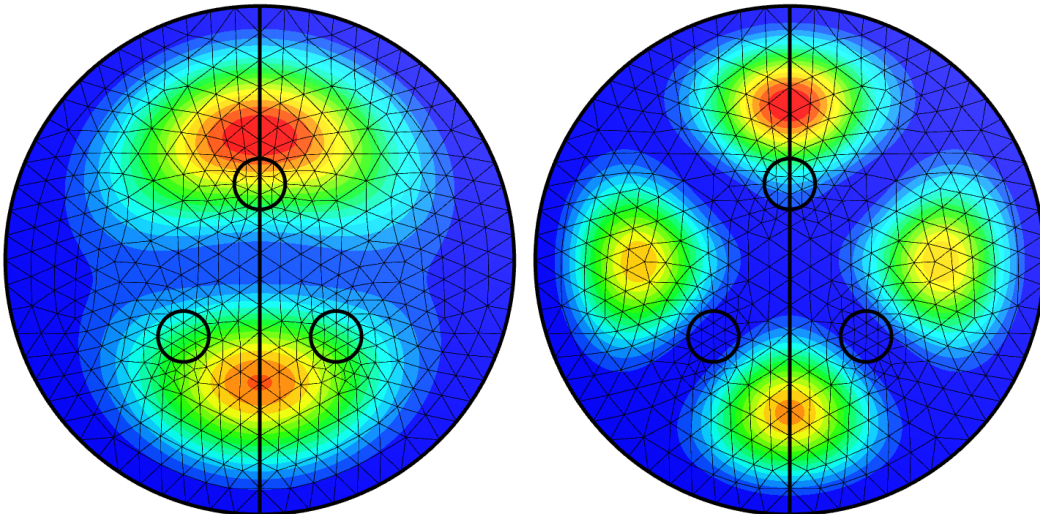

Figure 6: Two P symmetric intensities for $\rho, \tau = 0.1$, $d = 0.3$, whose eigenvalue solutions are 15.68 and 41.73.

come in complex conjugate pairs. To further confirm this, we calculated many eigenvalues for a fixed γ. Specifically, in Figure 5, we show the spectrum for $\gamma = 100$, computed using a Lagrange space X_h of polynomial degree $p = 4$. Clearly, many eigenvalues are complex and not all come in complex conjugate pairs.

Before concluding this section, we examine the intensities (square of the absolute values) of a few eigenmodes of $\mathcal{H}_h$, shown in Figure 6. These eigenmodes were obtained with parameters $p = 4, \rho = 0.1, d = 0.3, \tau = 0.3$ for eigenvalues $\lambda = 15.68$, and 41.73. We can note that both the eigenmodes are reflection symmetric. This is in accordance with the prior theory leading to Corollary 3.4, which predicted that eigenfunctions must be reflection symmetric.

7   Spectra from the PT-symmetric model

In this section, we present our computational findings on the spectra of the operator $\mathcal{A}_h$ defined in (21).

Again, we begin with the base case mentioned in Section 6, with V = 1 from (15). In Figure 7, we track (real and imaginary parts of) the lowest seven eigenvalues as a function of the parameter γ. Note that all eigenvalue bands at $\gamma = 0$ start at the values listed in (23). While the eigenvalues do vary as γ increases, initially they all remain real. This is quite unlike the behavior we saw in the P-symmetric case example of Figure 4.

As γ is increased further, at some critical *threshold* value of γ, often called the "breaking threshold", some eigenvalues become complex, as seen in Figure 7. It is also clear from the plot of the imaginary parts in the same figure that once they become complex, they actually occur in complex conjugate pairs. This is unlike the behavior in the previous Figure 4. However, it is entirely in accordance with the theory in Proposition 4.3. Note, that the first three eigenvalue bands in Figure 7 did not exhibit complex bifurcations in the range of γ considered. However, a few of the eigenvalues higher up in the spectrum exhibited breaking thresholds at what appear to be "exceptional points." We will define an exceptional point later, in Section 8.

An unusual finding in Figure 7 is the presence of multiple *re-entrant* points. Namely, after the few real eigenvalues have bifurcated into the complex plane, by further increasing the gain-loss parameter γ, one can apparently make them purely real again, at a higher value of γ, called the re-entrant point. This phenomena occurs for multiple eigenbands in Figure 7. To show this clearly, we have included zoomed in two-dimensional views in Figures 7b–7c as well as three-dimensional views for the same data in Figure 8.

Next, we see an example of how eigenfunctions change as γ is varied. We focus on the case where $d = 0.15 \times 2$, shown in Figure 7. Consider the two bands of real eigenvalues meeting at a bifurcating threshold in Figure 7b, after which they become complex conjugates. Denoting the corresponding two eigenfunctions by u_1 and u_2, we can examine their progression as γ increases through the bifurcating value. For each eigenfunction u, we plot its intensity $|u|^2$ in Figure 9 for selected γ-values. We conclude from Figure 9 that before the bifurcation, in accordance with the statement of Proposition 4.3 for real eigenvalues λ with one-dimensional eigenspace, the corresponding eigenfunction u is PT-symmetric, i.e., PTu and u are collinear, so *their intensities are P-symmetric, or reflection symmetric.* We see
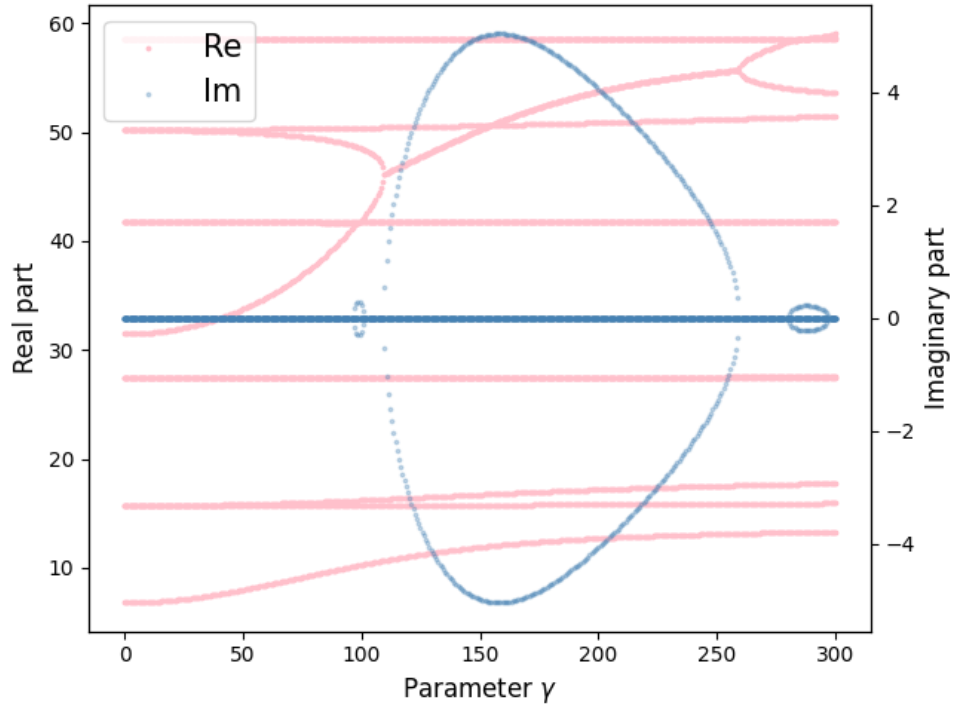
(a) Eigenvalue bands showing the variations in the lowest seven eigenvalues as the gain-loss parameter γ increases
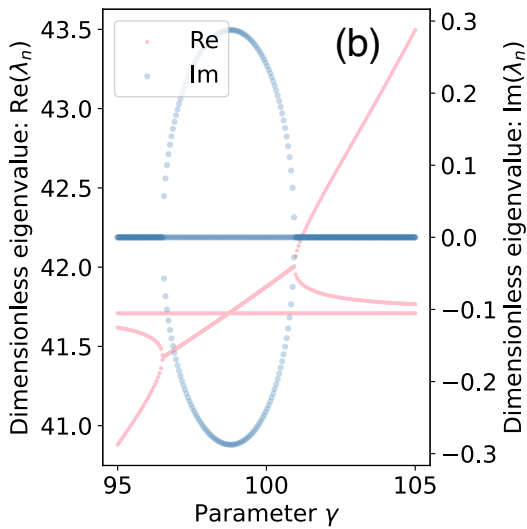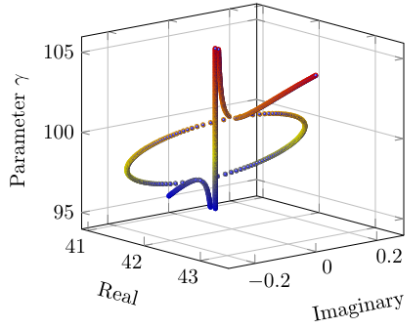

(b) Rescaled plot, zooming into the first bifurcation (the first oval in Figure 7a)
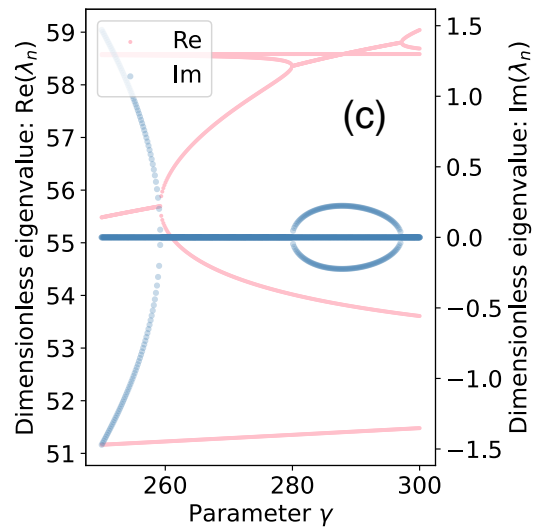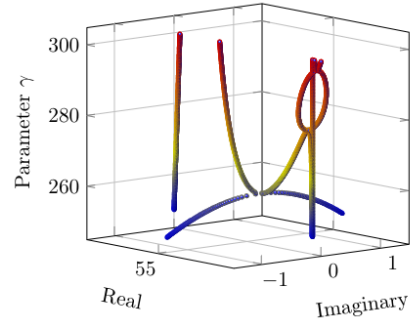

(c) Rescaled plot, zooming into the last part of Figure 7a

Figure 7: Multiple eigenvalue bifurcations for the case $d = 0.15 \times 2$, $\rho = 0.1$.

(a) 3D plot of data in Figure 7b (b) 3D plot of data in Figure 7c

Figure 8: 3D visualization composed of eigenvalues in the complex plane for each γ-value.
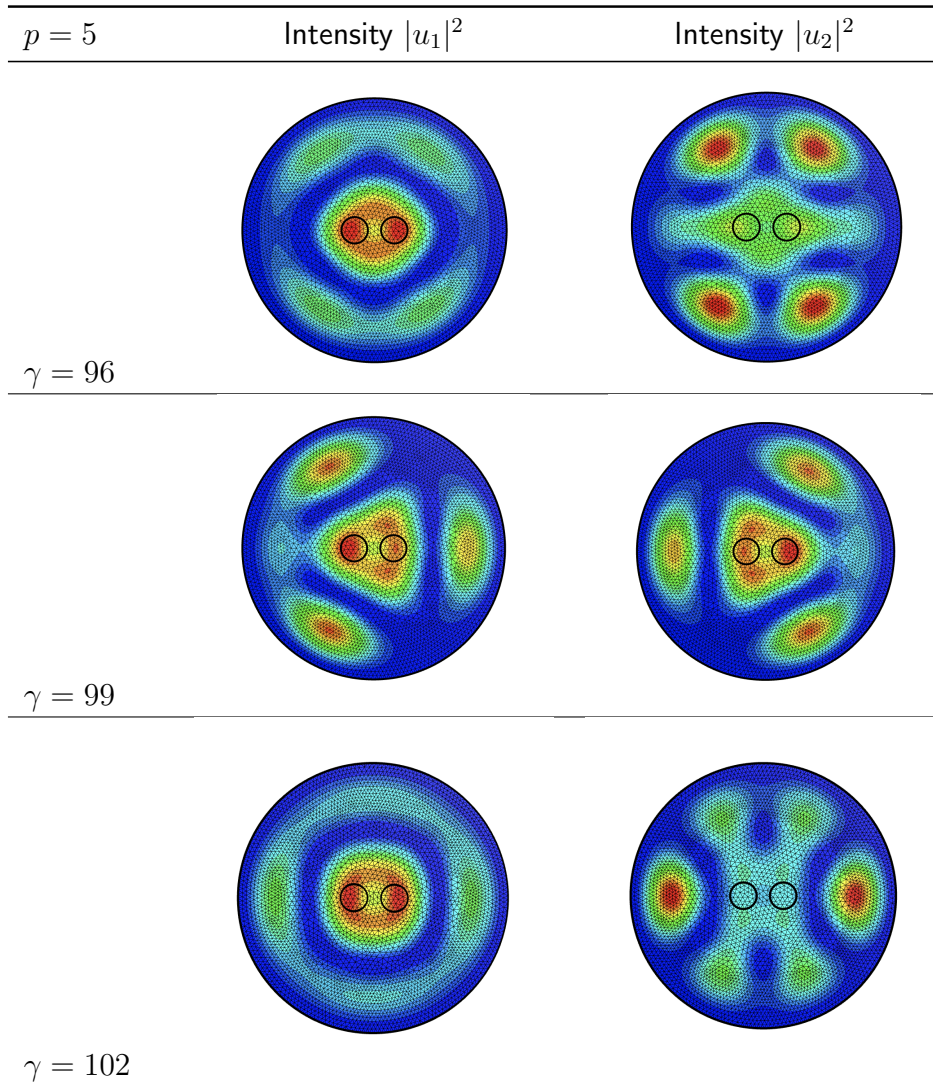

Figure 9: Two eigenfunctions around the first breaking threshold (where the eigenvalues become complex conjugate pairs) indicated in Figure 7b, where p is the polynomial degree.
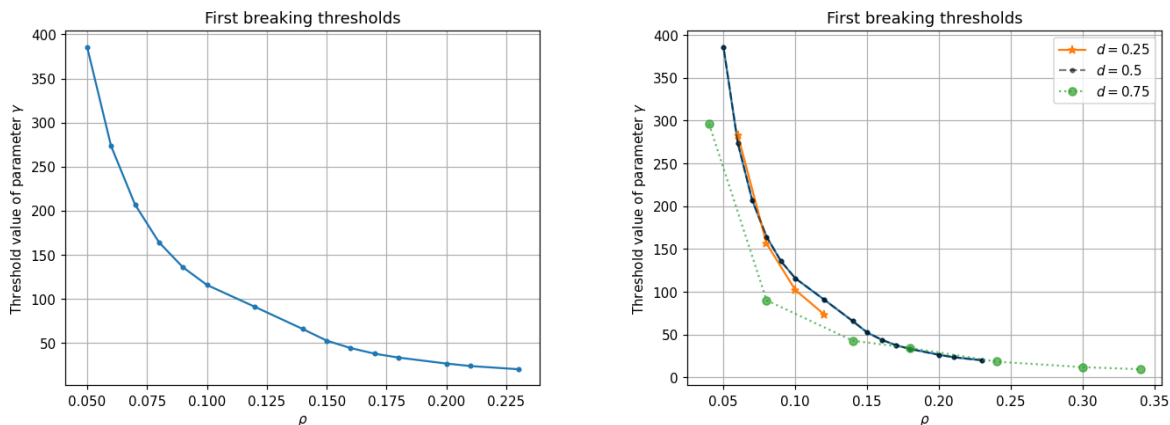
Figure 10: The changes in the first breaking threshold as the radius of gain-loss disks ρ is varied.

this reflection symmetry in the first row of plots of Figure 9 corresponding to $\gamma = 96$, before the breaking threshold, where λ is real. After the breaking threshold, in the plots of the second row for $\gamma = 99$, the intensities of the eigenmodes *no longer exhibit reflection symmetry.* This breakage of symmetry is the reason we refer to the threshold as a breaking threshold. This is also in accordance with the statement of Proposition 4.3 for non-real eigenvalues, which no longer guarantees that PTu and u are collinear, even if λ has a one-dimensional eigenspace. In fact, PTu must be linearly independent from u when λ is complex since it is an eigenfunction of a distinct eigenvalue $\bar{\lambda} \neq \lambda$, per Proposition 4.3. The final row of Figure 9 shows that the *reflection symmetry of intensities have been restored* after the re-entrant point when $\gamma = 102$.

Next, consider how *first breaking threshold* (often a quantity of practical interest) changes as the radius of the gain-loss disks, ρ, is varied. The results are in Figure 10. We observe an *inverse-square relationship* with ρ, in the left figure (where ρ is varied, fixing $d = 0.25$), and in the right figure (where ρ is varied, and we examine three different d values). It might be possible to explain such an inverse-square law by viewing the gain-loss disks as a distributed version of two points in the plane where gain and loss are concentrated. Reviewing the right graphs again, we anticipate complicated spectral variations with respect to d. For example, for the fixed value of $\rho = 0.1$ we note that from the different curves of the right figure, that the breaking threshold is *not a monotonic* function of d.

A more detailed picture of dependence of the first breaking threshold on d (the gain-loss separation) emerges from further extensive computations whose results are compiled in Figure 11. Here, d is varied, while $\rho = 0.1$. Note that the d values on the horizontal axis are nonuniformly and manually chosen (after seeing the first set of results) for better resolution of unanticipated variations. Note that in this figure, for values of $d < 2\rho$, the gain and loss disks overlap. We account for this overlap by careful meshing (such an overlapping case and accompanying mesh can be seen in Figure 12). Within the overlap, since gain and the loss cancel each other out, the values of V are real. It follows that the breaking thresholds
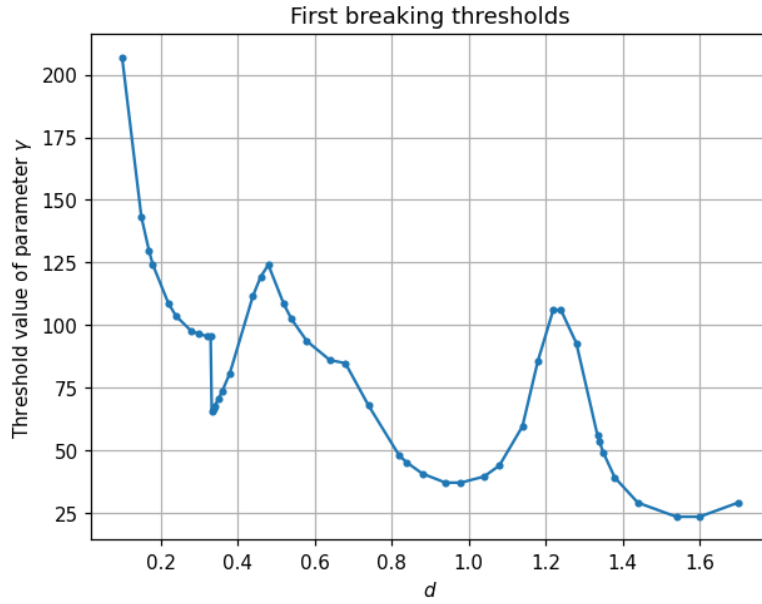
Figure 11: Variation of the first breaking thresholds with gain-loss separation distance d.

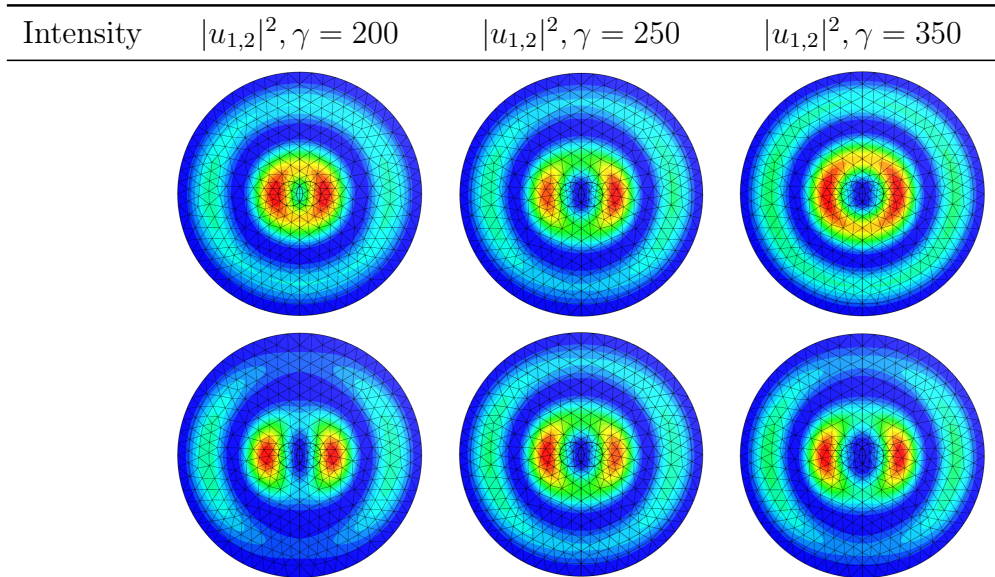| Intensity	$|u_{1,2}|^2, \gamma = 200$	$|u_{1,2}|^2, \gamma = 250$	$|u_{1,2}|^2, \gamma = 350$

Figure 12: Overlapping gain-loss disks corresponding to the case $d = 0.15, p = 4, \rho = 0.1$. The symmetry breakage is still visible in the second column, although it is less pronounced when compared to the nonoverlapping case in Figure 9.
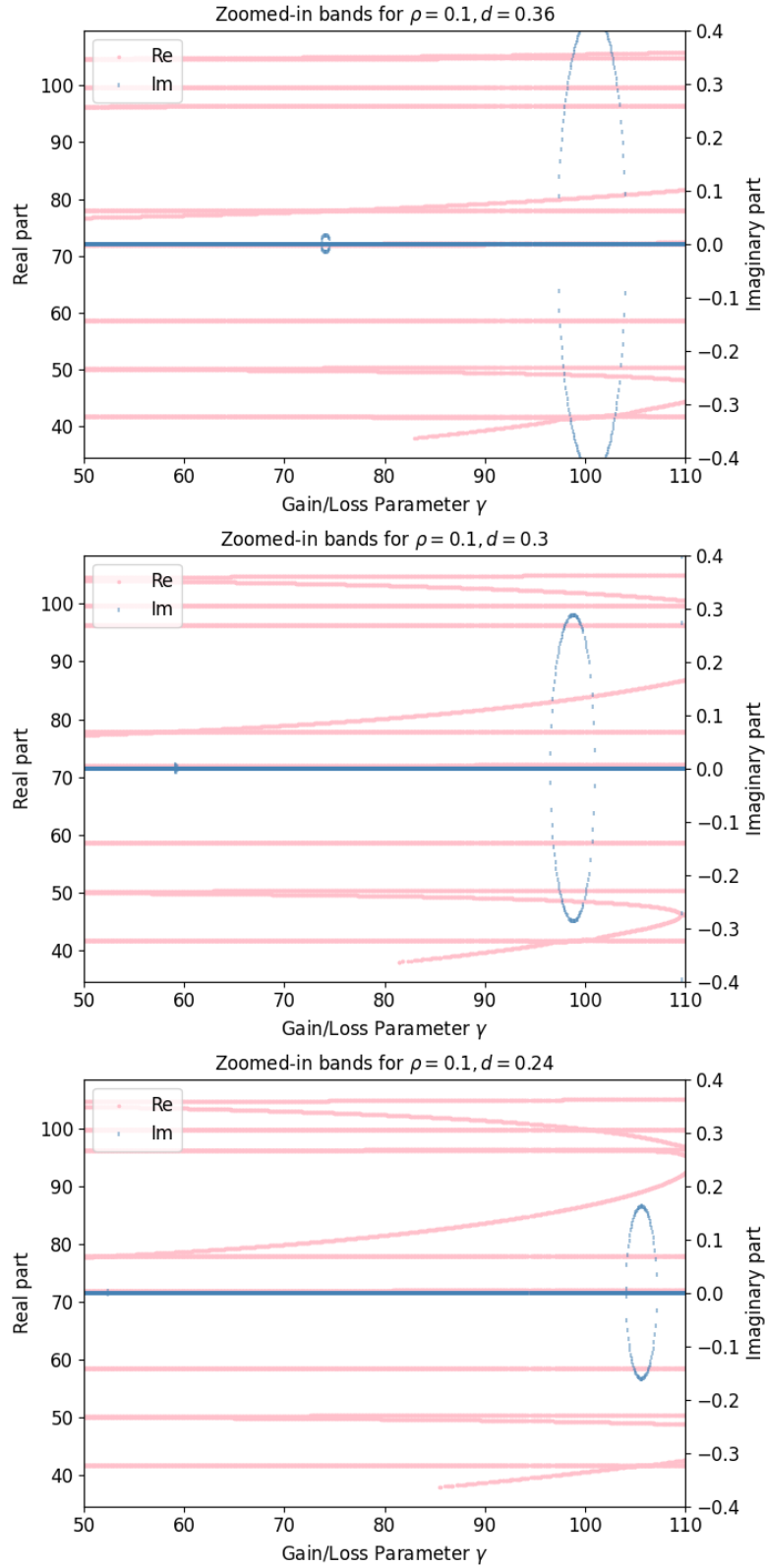
Figure 13: As gain-loss separation distance d decreases, the initial threshold identified as the first breaking threshold disappears, and the second becomes the first.

are high (as seen in the figure for low d values), determined by slivers of gain and loss left by the overlap. As d is increased, the overlap decreases (with no overlap when $d > 2\rho$). This explains the initial decay of the breaking threshold values. Nonetheless, the observed variations of the first breaking threshold as a function of d appears to be too complex for any one simplistic explanation. Some of the complexity is explained by multiple eigenvalues transitioning between the real and complex conjugate regimes as d varies.

For example, let us take a closer look at the apparent discontinuity in the above graph near $d = 0.3$. The eigenflows in Figure 13 identify the cause of this jump as the *disappearance of a bifurcation-reentrant loop* as d decreases, i.e., the initial first breaking threshold yielded by this loop disappears, so the second breaking threshold a higher γ value suddenly becomes the first breaking threshold.

8 Exceptional points

In the previous section, we have seen "breaking thresholds" occurring at specific parameter values for a selected PT-symmetric model. This model, after finite element discretization, typically creates numerical eigenproblems of size $10^4 \times 10^4$ or larger. It is difficult to distill the mathematical behavior at the thresholds due to the size of the problem. Therefore, in this section, through small (hand-computable) examples, we will find similar behavior at points called *exceptional points* in the mathematical literature (defined below). This allows us to better understand and place the behavior of the eigenflows shown in Section 7 into a mathematically known context.

Let us define

$$s(\gamma) := \text{the number of distinct eigenvalues of } T(\gamma).$$

It is known from analytic function theory [25], [37] that $s(\gamma)$ is a constant function on compact subsets of the domain of analyticity of $T(\gamma)$, *except* at a finite number of points, which we define as *exceptional points*, or EPs, where $s(\gamma)$ may take a different value.

For large eigenproblems, determining numerically whether a point is an exceptional point is problematic; finite computational searches will likely miss EPs, as they are just a few finitely many points in an infinite continuum of points where $s \equiv$ constant. Therefore, we focus on small analytic matrices $T(\gamma)$ for which all details are amenable to hand calculation, so no numerical search is involved. We proceed to demonstrate the behavior near exceptional points visually through some small examples.

Example 8.1. Let $T(\gamma)$ be defined by [25, Example 1.1(a)]

$$\begin{bmatrix} 1 & \gamma \\ \gamma & -1 \end{bmatrix}.$$

Its eigenvalues are

$$-\sqrt{\gamma^2 + 1}, \quad +\sqrt{\gamma^2 + 1}.$$

Clearly, we see that $s(\gamma)$ of this example is 2, except for at two exceptional points, $\pm i$.

To visualize the exceptional points in the continuum of remaining eigenvalues, we let $t \in \mathbb{R}$, and consider $\lambda_\pm(\gamma(t))$, along the curve $\gamma(t) = it$, a curve in the complex plane that
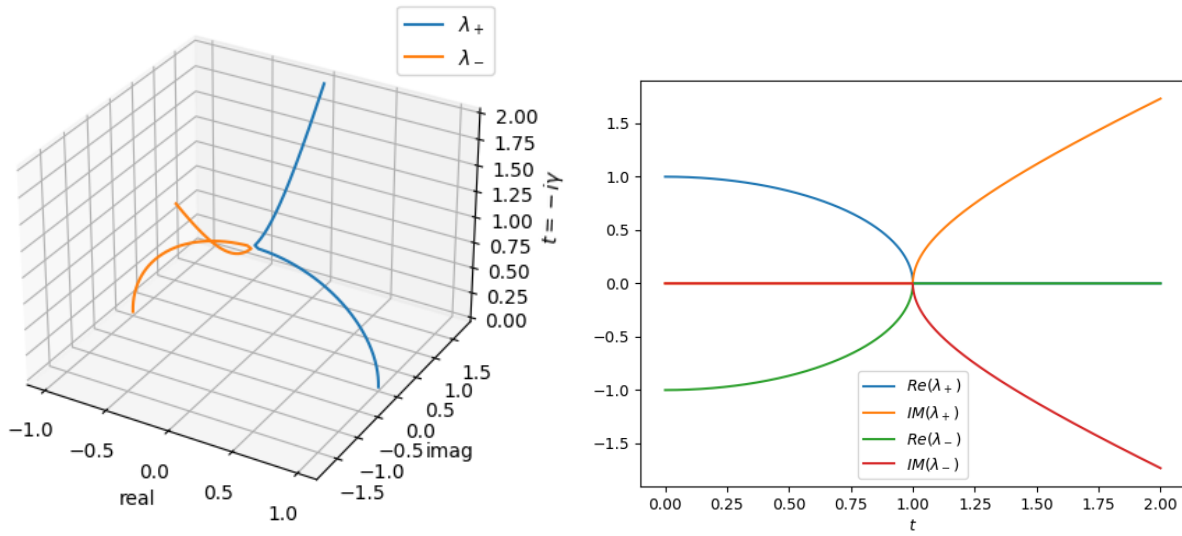
Figure 14: A visualization on the parameterized complex plane (right), as well as two-dimensional plot of the real and imaginary parts of $\lambda_\pm(\gamma(t))$, as a function of t, along $\gamma(t) = it$ (left).
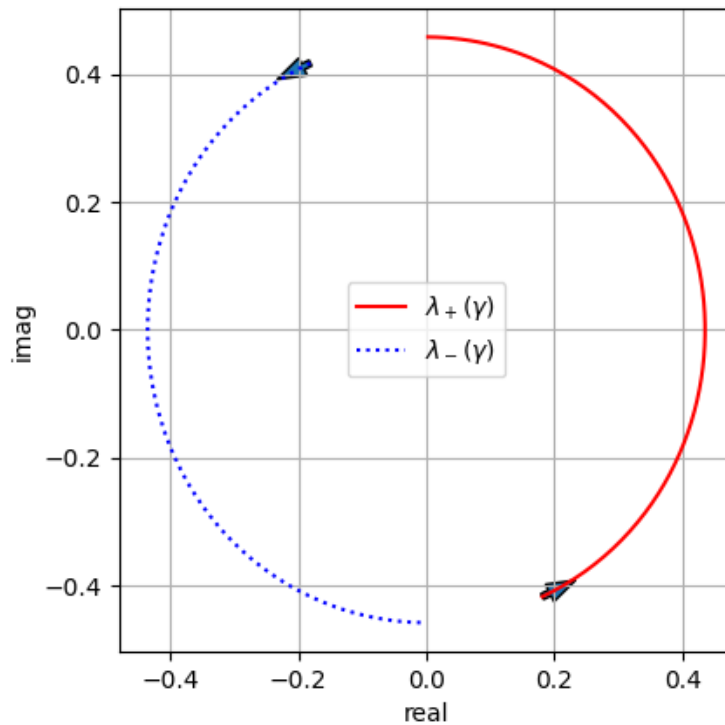

Figure 15: We see how $\lambda_+(\gamma(t))$ becomes $\lambda_-(\gamma(t))$ as the parameter t increases. A similar change occurs for $\lambda_-(\gamma(t))$. This signifies that as the cycle is traversed, the ordered eigenvalue set undergoes a permutation.

passes through both EPs. Then, $\lambda_\pm(\gamma(t))$ can be visualized as curves in three dimensional plots where the xy-plane represents $\mathbb{C}$ and the z axis represents parameter t. The first plot of Figure 14 gives such a visualization. Another way to visualize the eigenvalues is to plot the real and imaginary parts of the $\lambda_\pm(\gamma(t))$ as a function of t. This is shown in the second plot of Figure 14. Clearly, both these plots show *bifurcation behaviors* that are similar to the behavior near the symmetry breaking thresholds we have seen in the eigenflows of the previous section (such as Figure 7).

This example also shows additional interesting behavior near its exceptional point, as pointed out in [25]. *Eigenvalues can undergo a reordering along a path which encircles an exceptional point.* We can visualize this phenomenon in this example by examining how eigenvalues change along a different curve, this time circling around the exceptional point $+i$, namely,

$$\gamma(t) = i + \varepsilon e^{it},$$

for some small $\varepsilon > 0$. As we traverse this path around i, the eigenvalue trajectories $\lambda_\pm(\gamma(t))$ encircle zero, as shown in Figure 15. More interestingly, the ordered tuple of eigenvalues $(\lambda_-(\gamma(t)), \lambda_+(\gamma(t)))$ reverses its order after encircling half the path around zero.

Finally, we consider the eigenvectors near an exceptional point. Diagonalizing $T(\gamma)$ as the product of VDV^{-1}, we obtain

$$V = \begin{bmatrix} \frac{1-\sqrt{\gamma^2+1}}{\gamma} & \frac{\sqrt{\gamma^2+1}+1}{\gamma} \\ 1 & 1 \end{bmatrix}.$$

We see that eigenvectors, which are the columns of V, become collinear at the exceptional points of this example. For instance, at $\gamma = +i$,

$$V = \begin{bmatrix} -i & -i \\ 1 & 1 \end{bmatrix}.$$

This shows that in this example's EP, *geometric multiplicity is strictly less than algebraic multiplicity*. Namely, the former reduces to 1 at the EP, while the latter remains at 2. However, as we shall see not all exceptional points show this reduction in geometric multiplicity.

Example 8.2. This is a simpler example, from [25, Example 1.1(b)], which we include to show that a *reduction in geometric multiplicity does not need to occur at an EP*. Let $T(\gamma)$ be defined by

$$\begin{bmatrix} 0 & \gamma \\ \gamma & 0 \end{bmatrix}.$$

Its eigenvalues are

$$-\gamma, \quad +\gamma.$$

Once again, we see that $s(\gamma)$ of this example is 2, except at $\gamma = 0$, meaning there is one exceptional point. We can see by diagonalizing $T = VDV^{-1}$, that the eigenvectors of T can be chosen independently of γ, as the columns of

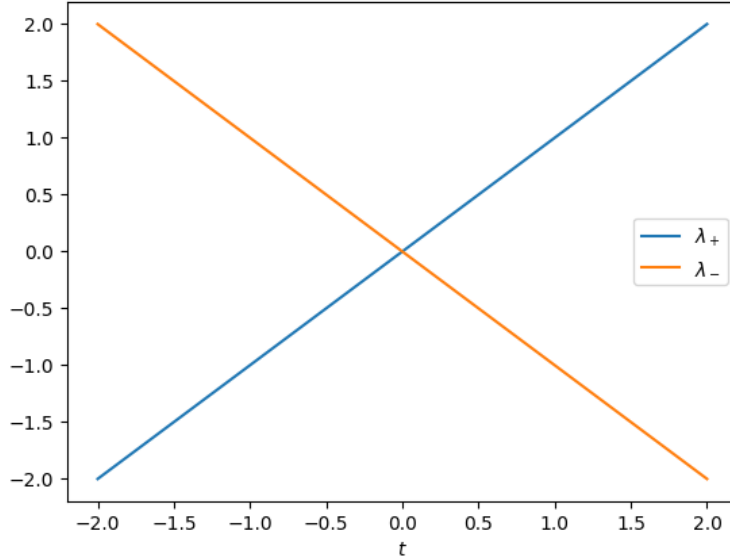$$V = \begin{bmatrix} -1 & 1 \\ 1 & 1 \end{bmatrix}.$$

Figure 16: The real and imaginary parts of $\lambda_{\pm}(it)$, as a function of t, along $\gamma(t)$.

Thus, the geometric multiplicity is always 2, as there are two linearly independent eigenvectors. Algebraic multiplicity must therefore be at least 2 (and is exactly 2), as T is 2×2. Therefore, unlike the previous example, we do not see any discrepancy between the geometric and algebraic multiplicities in this example.

A visualization of the two eigenvalues along the path

$$\gamma(t) = t,$$

which includes the exceptional point, is shown in Figure 16.

Example 8.3. Another simple example is offered by $T(\gamma)$ be defined by

$$\begin{bmatrix} 0 & \gamma \\ 0 & 0 \end{bmatrix},$$

mentioned in both [25, Example 1.1(c)] and [38, Example 2.9]. Clearly, the eigenvalues here are 0 for all γ. This means $s(\gamma) \equiv 1$ for all γ. This is an example of $T(\gamma)$ with *no exceptional points*. Note, the algebraic multiplicity of the zero eigenvalue is two for all γ. Additionally, note that $T(\gamma)$ *is permanently degenerate,* as $s(\gamma) < 2$ (recall that a square $N \times N$ matrix-valued function $T(\gamma)$ is said to be permanently degenerate when $s(\gamma) < N$).

Example 8.4. A closely related example is the $T(\gamma)$ defined by [25, Example 1.1(d)]

$$\begin{bmatrix} 1 & \gamma \\ 0 & 0 \end{bmatrix}.$$

The eigenvalues are the diagonal entries again, but this time, there are two distinct eigenvalues 0 and 1, no matter the value of γ . Hence the matrix is *not permanently degenerate. There are no exceptional points.* Thus, taking into account Example 8.3 also, the lack of exceptional points is not correlated with the operator being permanently degenerate.
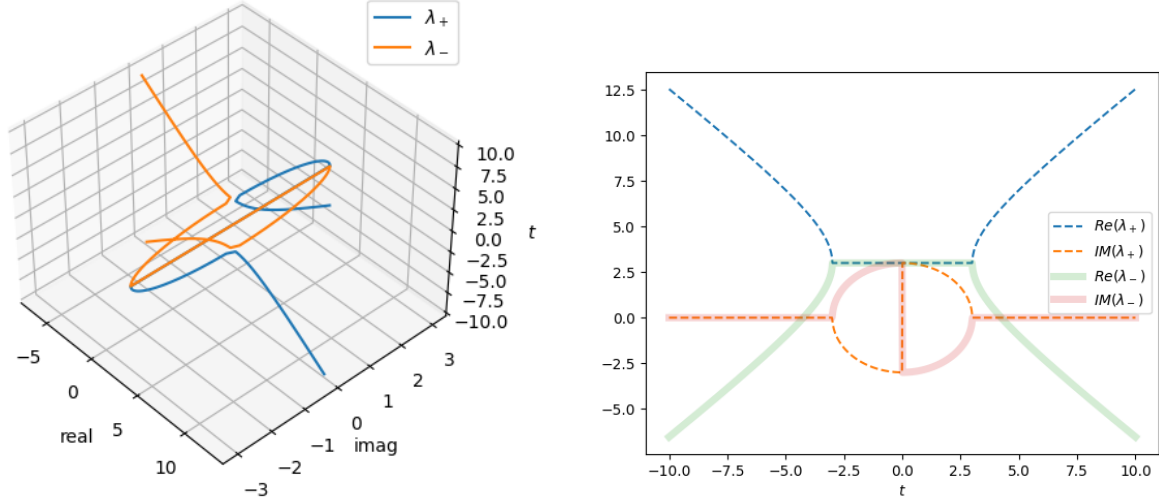
26

Figure 17: Visualization of the spectrum near an EP of Example 8.6. $\lambda_\pm(\gamma(t))$, when $\gamma(t) = t$ (left). Visualization on the parameterized complex plane (right), as well as two-dimensional plots of the real and imaginary parts of $\lambda_\pm(\gamma(t))$, when $\gamma(t) = t$ (left).

Example 8.5. Yet another similar example is the $T(\gamma)$ defined by [25, Example 1.1(f)]

$$\begin{bmatrix} \gamma & 1 \\ 0 & 0 \end{bmatrix}.$$

The eigenvalues are the diagonal entries again, namely 0 and γ, both analytic functions of γ in the entire complex plane. The number of distinct eigenvalues is $s(\gamma) \equiv 2$, except at the exceptional point $\gamma = 0$.

Example 8.6. Consider the $T(\gamma)$ defined by

$$\begin{bmatrix} \varepsilon + \gamma & \rho e^{i\alpha} \\ -\rho e^{-i\alpha} & \varepsilon - \gamma \end{bmatrix},$$

for $\varepsilon, \rho, \alpha \neq 0$. This example [38, Example 2.10] arises from a simplified model of unidirectional invisibility made possible using PT symmetry. Its eigenvalues are

$$\varepsilon + \sqrt{\gamma^2 - \rho^2}, \varepsilon - \sqrt{\gamma^2 - \rho^2}, \tag{24}$$

and corresponding eigenvectors are

$$\begin{bmatrix} \left(-\gamma + \sqrt{(\gamma^2 - \rho^2)}\right)\rho^{-1}e^{i\alpha} \\ 1 \end{bmatrix}, \quad \begin{bmatrix} \left(-\gamma - \sqrt{(\gamma^2 - \rho^2)}\right)\rho^{-1}e^{i\alpha} \\ 1 \end{bmatrix}. \tag{25}$$

We see from (24) that $s(\gamma) = 2$, except when $\gamma = \pm|\rho|$, which are the exceptional points. At these EPs, it is clear from (25) that the geometric multiplicity reduces to 1.

Next, fixing $\varepsilon = \rho = \alpha = 3$, let us visualize the spectral behavior near an EP. Consider $\lambda_\pm(\gamma(t))$, along the real line $\gamma(t) = t$, which passes through the EPs. Two types of

visualization (as explained in Example 8.1) of the resulting spectral variations are shown in Figure 17.

From the plots of Figure 17, we clearly see a bifurcation of the spectra from real to complex conjugates at $\gamma(t) = t = -|\rho| = -3$ and a re-entry from complex conjugates to real spectrum at $\gamma(t) = t = +|\rho| = +3$. This is similar to the behavior in Figure 7 for the higher dimensional eigenproblem we studied numerically. In the first plot of Figure 17, λ_- (orange) overlaps λ_+ (blue), and $\text{Im}(\lambda_-)$ (orange) overlaps $\text{Im}(\lambda_+)$ (red) in the second plot. In the second plot, the overlaps are seen more clearly. Additionally second plot shows a sudden switching between the imaginary parts of λ_+ and λ_- that occurs midway through the complex conjugate region.

Through these examples, we have seen that the behavior of the large and more complicated eigenproblems, unearthed in the previous section through extensive numerical studies, can also be reproduced, to some extent, in small 2×2 examples. In particular, we found analogs of both breaking thresholds and re-entrant points through the study of exceptional points of analytic 2×2 matrix functions.

Acknowledgments

References

[1] C. M. Bender, D. C. Brody, and H. F. Jones, "Complex extension of quantum mechanics," **Phys. Rev. Lett.**, vol. 89, p. 270 401, 27 Dec. 2002. DOI: 10.1103/PhysRevLett.89.270401. [Online]. Available: https://link.aps.org/doi/10.1103/PhysRevLett.89.270401.

[2] A. Mostafazadeh, "Pseudo-hermiticity versus PT symmetry: The necessary condition for the reality of the spectrum of a non-hermitian hamiltonian," **Journal of Mathematical Physics**, vol. 43, no. 1, pp. 205–214, Jan. 2002. DOI: 10.1063/1.1418246. [Online]. Available: https://doi.org/10.1063/1.1418246.

[3] A. Mostafazadeh, "Exact PT-symmetry is equivalent to Hermiticity," **Journal of Physics A: Mathematical and General**, vol. 36, no. 25, pp. 7081–7091, 2003, ISSN: 03054470. DOI: 10.1088/0305-4470/36/25/312.

[4] A. Mostafazadeh, "Pseudo-hermitian representation of quantum mechanics," **International Journal of Geometric Methods in Modern Physics**, vol. 07, no. 07, pp. 1191–1306, Nov. 2010. DOI: 10.1142/s0219887810004816. [Online]. Available: https://doi.org/10.1142/s0219887810004816.

[5] C. E. Rüter, K. G. Makris, R. El-Ganainy, D. N. Christodoulides, M. Segev, and D. Kip, "Observation of parity-time symmetry in optics," **Nature Physics**, vol. 6, no. 3, pp. 192–195, 2010, ISSN: 17452473. DOI: `10.1038/nphys1515`. eprint: `1003.4968`. [Online]. Available: `http://dx.doi.org/10.1038/nphys1515`.

[6] A. Regensburger, C. Bersch, M.-A. Miri, G. Onishchukov, D. N. Christodoulides, and U. Peschel, "Parity–time synthetic photonic lattices," **Nature**, vol. 488, no. 7410, pp. 167–171, Aug. 2012. DOI: `10.1038/nature11298`. [Online]. Available: `https://doi.org/10.1038/nature11298`.

[7] X. Zhu, H. Ramezani, C. Shi, J. Zhu, and X. Zhang, "$\mathcal{PT}$-symmetric acoustics," **Phys. Rev. X**, vol. 4, p. 031042, 3 Sep. 2014. DOI: `10.1103/PhysRevX.4.031042`. [Online]. Available: `https://link.aps.org/doi/10.1103/PhysRevX.4.031042`.

[8] J. Schindler, A. Li, M. C. Zheng, F. M. Ellis, and T. Kottos, "Experimental study of active LRC circuits with PT symmetries," **Physical Review A - Atomic, Molecular, and Optical Physics**, vol. 84, no. 4, pp. 1–5, 2011, ISSN: 10502947. DOI: `10.1103/PhysRevA.84.040101`.

[9] T. Wang, J. Fang, Z. Xie, N. Dong, Y. N. Joglekar, Z. Wang, J. Li, and L. Luo, "Observation of two pt transitions in an electric circuit with balanced gain and loss," **The European Physical Journal D**, vol. 74, no. 8, Aug. 2020. DOI: `10.1140/epjd/e2020-10131-7`. [Online]. Available: `https://doi.org/10.1140/epjd/e2020-10131-7`.

[10] C. H. Lee, S. Imhof, C. Berger, F. Bayer, J. Brehm, L. W. Molenkamp, T. Kiessling, and R. Thomale, "Topolectrical circuits," **Commun Phys**, vol. 1, no. 1, Jul. 2018. DOI: `10.1038/s42005-018-0035-2`. [Online]. Available: `https://doi.org/10.1038/s42005-018-0035-2`.

[11] Y. Ashida, Z. Gong, and M. Ueda, "Non-hermitian physics," **Advances in Physics**, vol. 69, no. 3, pp. 249–435, Jul. 2020. DOI: `10.1080/00018732.2021.1876991`. [Online]. Available: `https://doi.org/10.1080/00018732.2021.1876991`.

[12] Y.-X. Wang and A. A. Clerk, "Non-hermitian dynamics without dissipation in quantum systems," **Phys. Rev. A**, vol. 99, p. 063834, 6 Jun. 2019. DOI: `10.1103/PhysRevA.99.063834`. [Online]. Available: `https://link.aps.org/doi/10.1103/PhysRevA.99.063834`.

[13] F. Klauck, L. Teuber, M. Ornigotti, M. Heinrich, S. Scheel, and A. Szameit, "Observation of $\mathcal{PT}$-symmetric quantum interference," **Nature Photonics**, vol. 13, no. 12, pp. 883–887, Sep. 2019. DOI: `10.1038/s41566-019-0517-0`. [Online]. Available: `https://doi.org/10.1038/s41566-019-0517-0`.

[14] J. Li, A. K. Harter, J. Liu, L. de Melo, Y. N. Joglekar, and L. Luo, "Observation of parity-time symmetry breaking transitions in a dissipative floquet system of ultracold atoms," **Nature Communications**, vol. 10, no. 1, Feb. 2019. DOI: `10.1038/s41467-019-08596-1`. [Online]. Available: `https://doi.org/10.1038/s41467-019-08596-1`.

[15] L. Ding, K. Shi, Q. Zhang, D. Shen, X. Zhang, and W. Zhang, "Experimental determination of $\mathcal{PT}$-symmetric exceptional points in a single trapped ion," **Phys. Rev. Lett.**, vol. 126, p. 083 604, 8 Feb. 2021. DOI: 10.1103/PhysRevLett.126.083604. [Online]. Available: https://link.aps.org/doi/10.1103/PhysRevLett.126.083604.

[16] A. Quinn, J. Metzner, J. E. Muldoon, I. D. Moore, S. Brudney, S. Das, D. T. C. Allcock, and Y. N. Joglekar, **Observing super-quantum correlations across the exceptional point in a single, two-level trapped ion**, 2023. arXiv: 2304.12413 [quant-ph].

[17] C. M. Bender and S. Boettcher, "Real spectra in non-hermitian hamiltonians having $\mathcal{PT}$ symmetry," **Phys. Rev. Lett.**, vol. 80, pp. 5243–5246, 24 Jun. 1998. DOI: 10.1103/PhysRevLett.80.5243. [Online]. Available: https://link.aps.org/doi/10.1103/PhysRevLett.80.5243.

[18] M. Znojil, "$\mathcal{PT}$-symmetric square well," **Physics Letters A**, vol. 285, no. 1-2, pp. 7–10, Jun. 2001. DOI: 10.1016/s0375-9601(01)00301-2. [Online]. Available: https://doi.org/10.1016/s0375-9601(01)00301-2.

[19] Y. N. Joglekar and B. Bagchi, "Competing $\mathcal{PT}$ potentials and the re-entrant $\mathcal{PT}$-symmetric phase: A particle in a box," **Journal of Physics A: Mathematical and Theoretical**, vol. 45, no. 40, p. 402 001, Sep. 2012. DOI: 10.1088/1751-8113/45/40/402001. [Online]. Available: https://doi.org/10.1088/1751-8113/45/40/402001.

[20] L. Jin and Z. Song, "Solutions of $\mathcal{PT}$-symmetric tight-binding chain and its equivalent hermitian counterpart," **Phys. Rev. A**, vol. 80, p. 052 107, 5 Nov. 2009. DOI: 10.1103/PhysRevA.80.052107. [Online]. Available: https://link.aps.org/doi/10.1103/PhysRevA.80.052107.

[21] Y. N. Joglekar, D. Scott, M. Babbey, and A. Saxena, "Robust and fragile $\mathcal{PT}$-symmetric phases in a tight-binding chain," **Phys. Rev. A**, vol. 82, p. 030 103, 3 Sep. 2010. DOI: 10.1103/PhysRevA.82.030103. [Online]. Available: https://link.aps.org/doi/10.1103/PhysRevA.82.030103.

[22] Y. N. Joglekar, C. Thompson, D. D. Scott, and G. Vemuri, "Optical waveguide arrays: Quantum effects and PT symmetry breaking," **The European Physical Journal Applied Physics**, vol. 63, no. 3, p. 30 001, Sep. 2013. DOI: 10.1051/epjap/2013130240. [Online]. Available: https://doi.org/10.1051/epjap/2013130240.

[23] F. Ruzicka, K. S. Agarwal, and Y. N. Joglekar, "Conserved quantities, exceptional points, and antilinear symmetries in non-hermitian systems," **Journal of Physics: Conference Series**, vol. 2038, no. 1, p. 012 021, Oct. 2021. DOI: 10.1088/1742-6596/2038/1/012021. [Online]. Available: https://doi.org/10.1088/1742-6596/2038/1/012021.

[24] C. M. Bender, "PT symmetry in quantum physics: From a mathematical curiosity to optical experiments," **Europhysics News**, vol. 47, no. 2, pp. 17–20, Mar. 2016. DOI: 10.1051/epn/2016201. [Online]. Available: https://doi.org/10.1051/epn/2016201.

[25] T. Kato, **Perturbation theory for linear operators** (Classics in Mathematics). Berlin: Springer-Verlag, 1995.

[26] M.-A. Miri and A. Alù, "Exceptional points in optics and photonics," **Science**, vol. 363, no. 6422, eaar7709, Jan. 2019. DOI: 10.1126/science.aar7709. [Online]. Available: https://doi.org/10.1126/science.aar7709.

[27] Ş. K. Özdemir, S. Rotter, F. Nori, and L. Yang, "Parity–time symmetry and exceptional points in photonics," **Nature Materials**, vol. 18, no. 8, pp. 783–798, Aug. 2019, ISSN: 1476-4660. DOI: 10.1038/s41563-019-0304-9. [Online]. Available: https://doi.org/10.1038/s41563-019-0304-9.

[28] T. Gratcheva, Y. N. Joglekar, and J. Gopalakrishnan, "PT-symmetry-enabled stable modes in multi-core fiber," **Physical Review Research (to appear)**, 2024.

[29] J. Gopalakrishnan, "MTH 65X Course Materials: Ready Reference and Lecture Notebooks," Portland State University, 2024. [Online]. Available: https://web.pdx.edu/~gjay/teaching/mth651_2023/651-jupyterlite/FEMnotebooks/0_INDEX.html.

[30] R. A. Adams and J. J. F. Fournier, **Sobolev spaces** (Pure and Applied Mathematics (Amsterdam)), Second. Elsevier/Academic Press, Amsterdam, 2003, vol. 140.

[31] A. Ern and J.-L. Guermond, **Finite Elements I**. Springer, 2021.

[32] J. Schöberl, "NETGEN – An advancing front 2D/3D-mesh generator based on abstract rules," **Comput. Visual. Sci**, vol. 1, pp. 41–52, 1997.

[33] J. Kestyn, E. Polizzi, and P. T. P. Tang, **Feast eigensolver for non-hermitian problems**, 2015. arXiv: 1506.04463 [math.NA].

[34] J. Gopalakrishnan, L. Grubišić, and J. Ovall, "Spectral discretization errors in filtered subspace iteration," **Mathematics of Computation**, vol. 89, no. 321, pp. 203–228, 2020. DOI: 10.1090/mcom/3483. [Online]. Available: https://doi.org/10.1090/mcom/3483.

[35] J. Gopalakrishnan **et al.**, **Pythonic FEAST**, https://bitbucket.org/jayggg/pyeigfeast, 2017.

[36] J. Schöberl **et al.**, **NGSolve**, http://ngsolve.org.

[37] Knopp, **Theory of functions, Part II**. Dover Publications Inc., 1947.

[38] Y. Ashida, Z. Gong, and M. Ueda, "Non-hermitian physics," **Advances in Physics**, vol. 69, no. 3, pp. 249–435, Jul. 2020, ISSN: 1460-6976. DOI: 10.1080/00018732.2021.1876991. [Online]. Available: http://dx.doi.org/10.1080/00018732.2021.1876991.